Physical characterization of thermally evaporated Sn–Sb–Se thin films for solar cell applications

Tunc Bektas[1,2] · Ozge Surucu[2] · Makbule Terlemezoglu[3] · Mehmet Parlak[1,4]

Abstract

The substitution of Sb in binary SnSe structure may lead to tailoring the physical properties of both SnSe and SbSe, promising absorber layers for thin film solar cells. The resulting Sn–Sb–Se structure could be an outstanding material for photovoltaic applications. In this study, Sn–Sb–Se thin films were deposited by thermal evaporation, and the effect of annealing on the films' structural, optical, and electrical properties were reported. XRD measurement shows that annealing at 300 °C yields the best crystalline quality, and structural parameters were calculated using XRD data. SEM and AFM measurements indicate deformation in the film surface after annealing at 400 °C. UV–Vis spectroscopy measurement provides a high absorption coefficient which indicates a direct band gap. The band gap and activation energies of the as-grown sample were found as 1.59 eV and 106.1 meV, respectively. The results of SEM, AFM, XRD, Raman, UV–Vis spectroscopy and temperature-dependent photoconductivity measurements were discussed throughout the paper.

1 Introduction

The growing energy demand and environmental issues, such as the limitation of natural sources and efforts to reduce greenhouse emissions, make renewable energy popular [1]. As well as other renewable energy sources (i.e., wind, geothermal, etc.), solar energy has an essential role in satisfying the energy demand [2]. Therefore, the photovoltaic (PV) industry seeks promising materials to benefit from solar energy efficiently. Several materials are used for PV applications, such as silicon (Si), CdTe- CdSe/S, and chalcopyrites (CIGS) or CZTSe/S [3–8]. Besides many advantages, these materials have disadvantages such as natural limitations,

expansiveness, non-abundancy, toxicity, instability, or phase formation difficulties [9–11]. As a result, cheap, stable, abundant, and less toxic materials gain importance for the future of the PV industry. Therefore, tin (Sn), antimony (Sb), and selenium (Se) based materials such as SnSe, SbSe, and CuSbSe are considered promising absorber layers for PV applications as well as their thermoelectric and infrared applications [12–17]. SbSe thin films have an orthorhombic structure and p-type conductivity [18, 19]. These films have a direct band gap in 1.10–1.55 eV interval [16, 18]. Moreover, Chen et.al. reported that it has an indirect band gap $E_{g,indirect} = 1.04$ eV, and a direct band gap $E_{g,direct} = 1.17$ eV [20]. Therefore, SbSe is properly used in PV applications due to the ideal band gap value, high absorption coefficient ($\sim 10^5$ cm^{-1}), and ease of fabrication using thermal evaporation, magnetron sputtering, spin coating, and chemical bath deposition, and laser pulse deposition methods [18, 21]. Similarly, SnSe thin films have an orthorhombic structure, high chemical stability, and p-type conductivity [22]. SnSe thin films also have a high absorption coefficient ($\sim 10^5$ cm^{-1}) and direct band gap in 1–1.5 eV interval [22, 23]. Moreover, Shikha et al. indicate that the direct band gap of SnSe thin films is in 1.50–1.91 eV interval [24]. Various coating methods such as chemical vapor deposition, thermal evaporation, chemical bath deposition, vacuum evaporation, and sol–gel methods are applicable to fabricate

✉ Ozge Surucu
ozge.surucu@atilim.edu.tr

1 Department of Physics, Middle East Technical University, 06800 Ankara, Turkey

2 Department of Electrical and Electronics Engineering, Atilim University, 06836 Ankara, Turkey

3 Department of Physics, Gazi University, 06560 Ankara, Turkey

4 Center for Solar Energy Research and Applications (GÜNAM), Middle East Technical University, 06800 Ankara, Turkey

SnSe thin films [25, 26]. SnSe may have an indirect band gap $E_{g,indirect} = 0.93–1.30$ eV depending on the deposition techniques [27].

In this study, we aimed to tailor the physical properties of SnSe and SbSe thin films and obtain the optically and electrically better absorber layers for photovoltaic applications. Sn–Sb–Se thin films were deposited by the thermal evaporation method from SnSbSe bulk crystal grown by a vertical Bridgman method in our previous study [28]. Thermal evaporation was considered the more stable way of coating by considering the evaporation temperatures of Sn, Sb, and Se elements. The SnSbSe powder, obtained from previously grown SnSbSe bulk crystal, evaporated in a vacuum chamber, and deposited at room temperature on soda-lime glass substrates cleaned by a chemical process and ultrasonic vibration. During the deposition, the deposition rate was kept between 0.9 and 1.2 Å/s to get rid of pinholes and obtain a uniform coating. The thickness of coated Sn-Sb–Se thin films was measured by DEKTAK profilometer as approximately 250 nm. To observe the effect of annealing on the physical properties of Sn-Sb–Se thin films, one of the films was kept as 'as grown,' and the others were annealed at 100 °C, 200 °C, 300 °C and 400 °C in nitrogen (N) environment for 30 min. To determine the surface properties, SEM images of Sn–Sb–Se thin films were obtained by Zeiss EVO 15 SEM. The atomic percentages of Sn, Sb, and Se atoms in each film were determined by EDAX measurement. The crystal structure of Sn–Sb–Se thin films was analyzed by XRD measurement using Rigaku Miniflex (Cu:Kα, $\lambda = 1.54$ Å) to calculate interplanar distance, dislocation density, stress and strain. The surface morphology and Raman spectra of the films were obtained by Veeco Multimode V atomic force microscopy (AFM) and Horiba-Jobin Yvon i550 spectrometer, respectively. The transmission measurements were carried out by Perkin Elmer—Lambda 45 UV–VIS Spectrometer to investigate. Then, indium (In) contacts were coated on each sample by thermal evaporation, and copper wires were attached to these contacts using silver paste for conductivity measurement. Conductivities of Sn–Sb–Se thin films were analyzed by NanoMagnetics Instruments- cryostat and Keithley 2401 Sourcemeter. Activation energies and resistivities were calculated using conductivity data, and the effect of annealing temperature on crystal structure, surface morphology, band gap, conductivity, and activation energy of Sn-Sb–Se thin film were reported.

2 Results and discussion

Figure 1 represents the EDS graphs of Sn–Sb–Se thin films. Only characteristic X-ray peaks of Sn, Sb, and Se elements were obtained in this figure. The unnamed peaks are the satellite peaks of Sn, and there is no contribution of other elements in EDS graphs [29]. This result indicates the purity of the samples.

Atomic percentages of Sn, Sb, and Se elements in as-grown and annealed Sn-Sb–Se thin films are given with ±2% detection error in Table 1. The increment in annealing temperature makes Sn-Sb–Se thin films Sn abundant and Se deficient. Since Se is the most volatile element in the structure, it may re-evaporate from the substrate during heat treatment depending on the high annealing temperature, and Se deficiency increases [30]. In addition, the increase in the atomic percentage of Sb at 100 ℃ can be attributed to the preferential sublimation of Sn and Se atoms from the single SnSbSe crystal source. As a result, the Sb atoms become more concentrated in the remaining thin film. However, it is observed that the atomic percentage of Sb remains almost constant for temperatures of 200 ℃, 300 ℃ and 400 ℃, which is an interesting observation. This phenomenon can be explained by the difference in the vapor pressures of Sn, Sb and Se atoms at different temperatures. At 100 ℃, the vapor pressure of Sn and Se atoms is higher than that of Sb atoms, which leads to a preferential sublimation of Sn and Se atoms and an increase in the atomic percentage of Sb. However, at higher temperatures, the vapor pressures of Sn and Se atoms decrease, and the vapor pressure of Sb atoms increases, resulting in a more uniform distribution of Sb atoms in the thin film.

SEM measurement was carried out to analyze the surface structure of as-grown and annealed Sn-Sb–Se thin films. Figure 1 indicates the SEM images of samples, and no crack appears on the film surface. Either as grown samples or the samples annealed at 100 °C, 200 °C and 300 °C have a smooth surface with no seen grains at this magnification. The small grain size of the surface structure may indicate high resistivity [31]. Furthermore, the SEM image of a sample annealed at 400 °C given in Fig. 1e exhibits a rough and deformed surface. The deformation at this annealing temperature may be attributed to the increased thermal stress on the structure due to the increasing annealing temperature.

The sample annealed at 300 °C has peaks at around 31.37 and 32.33° which correspond to (251) and (351) orientations with orthorhombic lattice structure according to ICDD Card No: 01-077-1672. The intensity of XRD peak belonging to the sample annealed at 400 °C is less than the sample annealed at 300 °C since 400 °C annealing deforms the structure, as seen in Fig. 2. As Kumar et al. indicates that SnSe thin films have better crystalline quality at 300 °C and the XRD peak becomes less intense after 325 °C [32]. Similarly, the Sn-Sb–Se crystal structure reaches its best form after annealing at around 300 °C. The interplanar distance (d), average grain size (D), the strain of lattice (ε), and dislocation density (δ) of the

Fig. 1 The EDS graphs, SEM and AFM images of Sn-Sb–Se thin films: as grown (**a**), annealed at 100 °C (**b**), at 200 °C (**c**), at 300 °C (**d**) and at 400 °C (**e**)
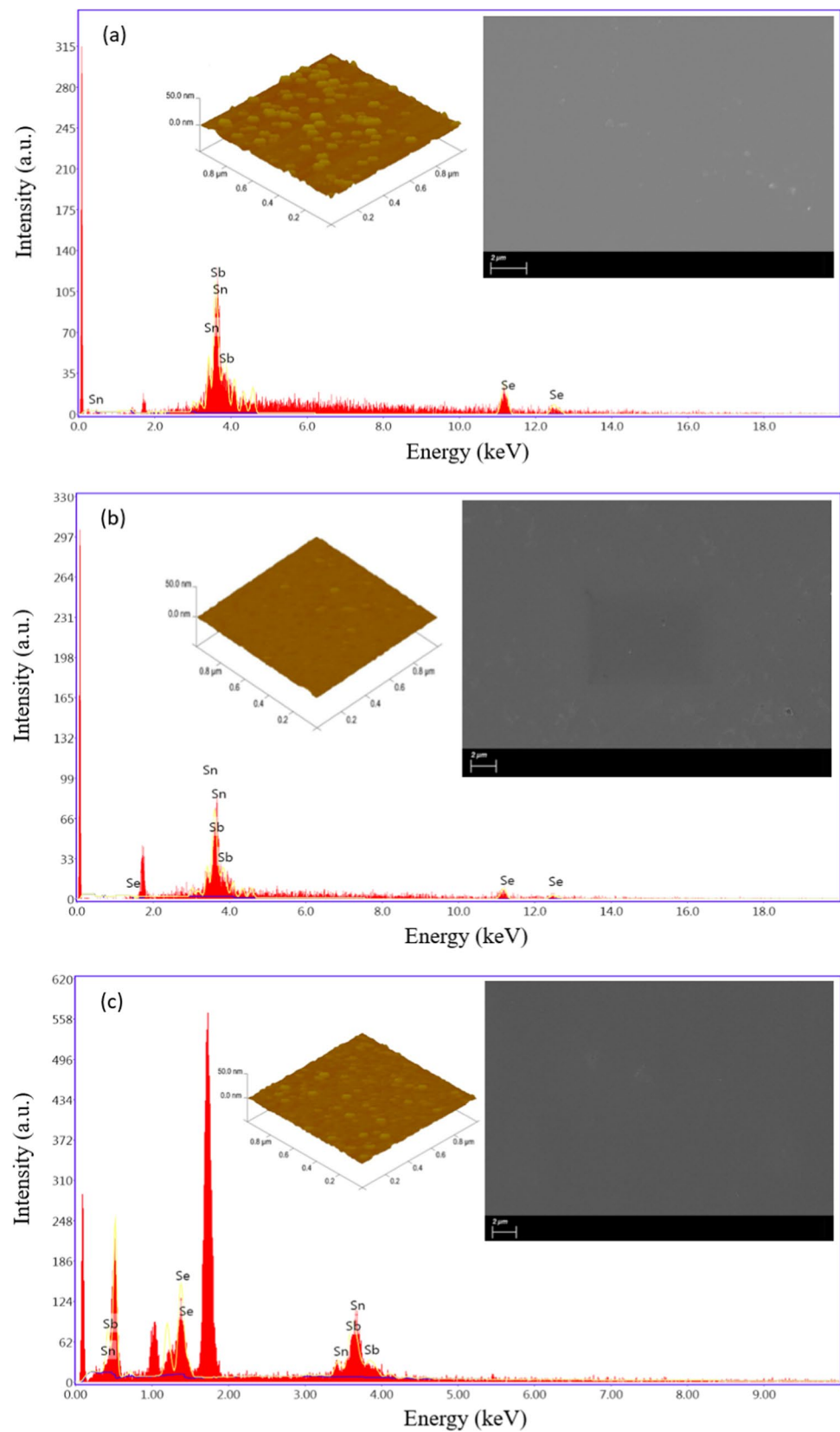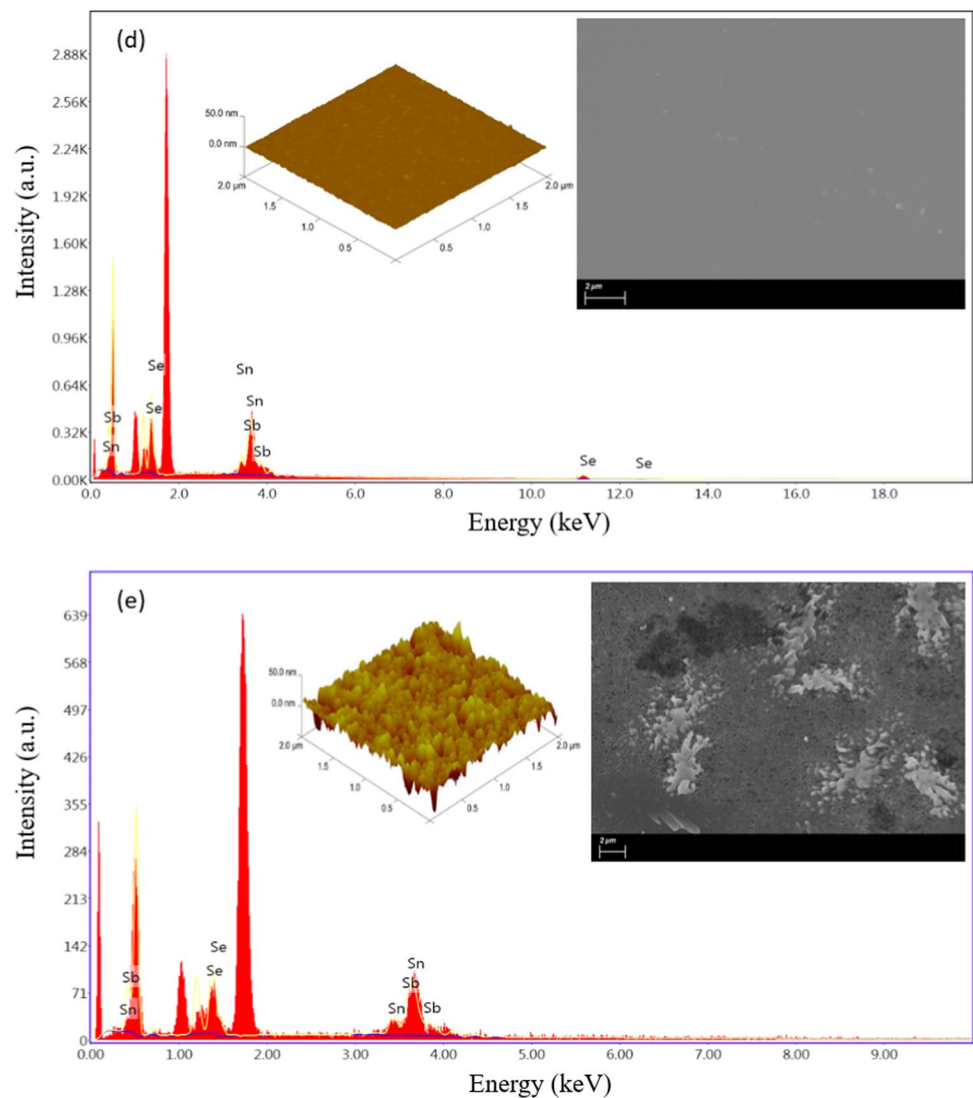
Fig. 1 (continued)

Table 1 The stoichiometry of as-grown and annealed samples

Samples	Sn%	Sb%	Se%
as grown	8.43 ± 0.17	16.83 ± 0.34	74.74 ± 1.49
annealed at 100 °C	11.69 ± 0.23	25.91 ± 0.53	64.40 ± 1.29
annealed at 200 °C	13.02 ± 0.26	32.49 ± 0.65	54.50 ± 1.09
annealed at 300 °C	17.26 ± 0.35	31.49 ± 0.63	51.25 ± 1.03
annealed at 400 °C	20.09 ± 0.40	30.64 ± 0.61	49.28 ± 0.99

samples having crystalline structure were calculated by using the following formulas and tabulated in Table 2.

$$n\lambda = 2d\sin\theta \tag{1}$$

$$D = \frac{K\lambda}{\beta\cos\theta} \tag{2}$$

$$\epsilon = \frac{\beta\cos\theta}{4} \tag{3}$$

$$\delta = \frac{1}{D^2} \tag{4}$$

Table 2 indicates that annealing at 400 °C yields more considerable interplanar distance and grain size as well as smaller strain and dislocation density. Despite the better structural parameters, a less intense peak is observed at this annealing temperature because of the deformed surface.

AFM measurement was carried out to investigate surface morphologies of as-grown and annealed Sn-Sb–Se thin films. Figure 1 shows that as-grown sample and the samples annealed at 100 °C and 200 °C have rough surfaces. Because annealing affects the grain size and shape, the surface roughness decreases as the annealing temperature increases. The sample annealed at 300 °C has the smoothest surface since
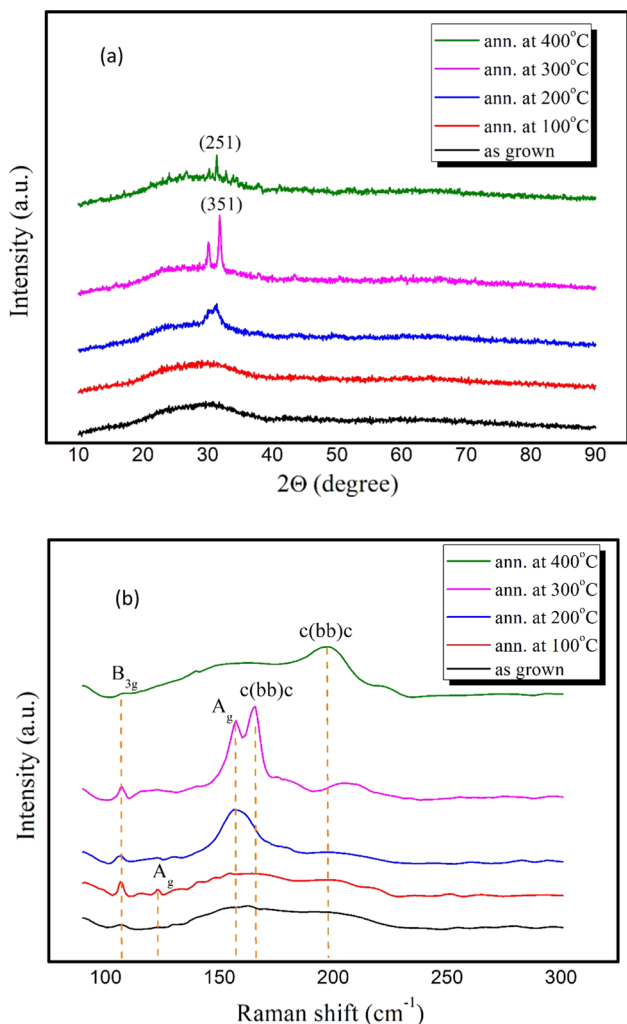
Fig. 2 XRD graphs (**a**) and Raman spectra (**b**) of as-grown and annealed Sn-Sb–Se thin films

Table 2 Structural parameters of samples having the crystalline structure

Samples	d (Å)	D (nm)	ε ($\times 10^{-2}$lin^{-2} m^{-4})	δ ($\times 10^{10}$cm^{-2})
annealed at 300 °C	2.77	35.74	10.0	7.8
annealed at 400 °C	2.85	49.91	7.25	4.0

the sample reaches the best crystalline quality at this temperature. However, the surface deformation due to high annealing temperature is clearly seen in Fig. 1e.

Figure 2 represents the Raman spectra of Sn-Sb–Se thin films as well. The dotted lines in this figure correspond to peak positions at 106.9, 157.1, and 165.3 cm^{-1}. The peak at 106.9 cm^{-1} may belong to B_{3g} mode of SnSe structure [25]. The peak at 157.1 cm^{-1} may be attributed to A_g^3 mode

of SnSe and A_{2u} mode of SbSe due to Sb-Sb interactions [33, 34]. The peaks at 165.3 cm^{-1} and 197 cm^{-1} correspond to c(bb)c vibration modes [35, 36].

Equation 5 is known as Beer-Lambert law, and it allows to express the absorption coefficient as a function of transmittance as given in Eq. 6, where d is the film thickness [37]. Inserting the absorption coefficient into Eq. 7 leads to calculating the optical band gap using '$(\alpha h\upsilon)^2$ vs. hυ' and '$(\alpha h\upsilon)^{1/2}$ vs. hυ' graphs for allowed direct and indirect transitions, respectively [38].

$$I = I_0 e^{-\alpha d} \tag{5}$$

$$\alpha = -\frac{1}{d} lnT \tag{6}$$

$$(\alpha h\upsilon)^{1/n} = A\left[h\upsilon - E_g\right] \tag{7}$$

Transmission measurements of Sn-Sb–Se thin films point out the absorption coefficient at 10^4 order, and only a direct optical band gap is observed after plotting both '$(\alpha h\upsilon)^2$ vs. hυ' and '$(\alpha h\upsilon)^{1/2}$ vs. hυ' graphs.

Figure 3 shows the Tauc plots of Sn–Sb–Se thin films. The band gap energy of each sample is determined by applying linear fits on a region where absorption starts. The energy band gap values are tabulated in Table 3.

As grown and 100 °C annealed samples have the same direct band gap energies, 1.59 eV and this shows that annealing at 100 °C could not create a change in lattice structure as verified by XRD graph in Fig. 2. Annealing at 200 °C causes a lattice expansion which yields a decrement in band gap energy. The band gap energies exhibit an increasing trend at 300 °C and 400 °C due to the shift of the absorption edge to the higher energies. This phenomenon is known as Burstein-Moss effect [39].

Temperature-dependent photoconductivity conductivity measurement of as grown Sn-Sb-Se thin film is given as Arhenius plot in Fig. 4. This measurement was analysed using Wilson's exponential law, given in Eq. 8, exhibits the conductivity and temperature relation [40]. In this equation, E, σ, and k represent activation energy, conductivity, and Boltzmann constant, respectively. This equation leads to calculate the activation energy from temperature-dependent conductivity data.

$$\sigma = \sigma_0 e^{-\frac{\Delta E}{kT}} \tag{8}$$

Using Eq. 8, activation energies of as-grown sample and the samples annealed at 100 °C, 200 °C, 300 °C and 400 °C are calculated as 106.1, 122.3, 126.5, 158.7, and
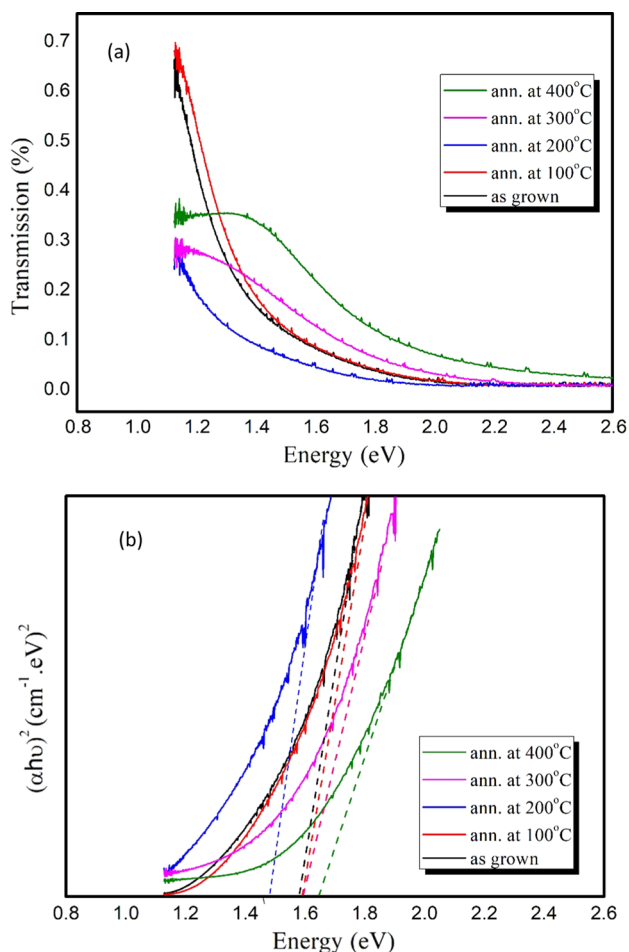
Fig. 3 Transmission spectrum (**a**) and $(\alpha h\upsilon)^2$ vs. $h\upsilon$ graph (**b**) of Sn–Sb–Se thin films

Table 3 Band gap energy (E_g) values of as-grown and annealed Sn–Sb–Se thin films

Samples	Band gap energy (eV)
as grown	1.59
annealed at 100 °C	1.59
annealed at 200 °C	1.49
annealed at 300 °C	1.60
annealed at 400 °C	1.67

151.0 meV, respectively. Furthermore, the temperature-dependent conductivity measurement carried out under illumination has intensities 20, 35, 55, 80 and 100 mW/cm^2, and it is observed that conductivity tends to increase under illumination.
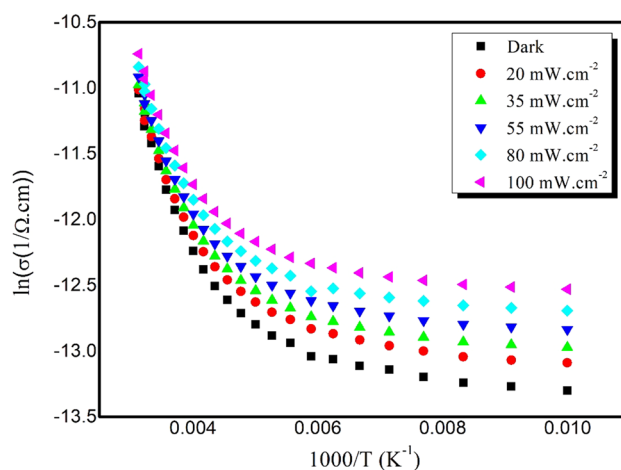
Fig. 4 Arrhenius plot of as-grown Sn–Sb–Se thin film

3 Conclusion

The deposition and characterization of Sn–Sb–Se thin films were reported in this paper. Thin film deposition was done out by thermal evaporation on the glass substrate. Then, samples were annealed at 100 °C, 200 °C, 300 °C and 400 °C for 30 min. Thickness measurement showed that the film thickness for each sample was approximately 250 nm, and film thickness was almost uniform through the film surface. The stoichiometry of as-grown and annealed samples were given, and the effect of annealing temperature on stoichiometry was discussed. SEM and AFM measurements exhibit that annealing at 400 °C resulted in deformation in the film surface, and the samples annealed at a temperature less than 400 °C have smooth surfaces. XRD measurement indicated that as-grown sample was amorphous and 100 °C annealing temperature did not provide enough thermal energy to construct a uniform crystal structure. Annealing at 300 °C showed better crystallinity. B_{3g}, A_g^3, and A_{2u} Raman modes were observed in Raman spectra. In addition, as-grown sample has 1.59 eV direct energy band gap, and the absorption coefficient is measured at $\sim 10^4$ cm^{-1} order. The effect of annealing on the band gap energies was investigated. Also, activation energies were reported in 250–330 °K intervals as a result of temperature-dependent photoconductivity measurement.

Data availability Data will be made available on request.

References

1. P. Zhao, Z. Lu, J. Fang, S.R. Paramati, K. Jiang, Determinants of renewable and non-renewable energy demand in China. Struct. Chang. Econ. Dyn. **54**, 202–209 (2020). https://doi.org/10.1016/j.strueco.2020.05.002

2. N. S. Lewis and D. G. Nocera, Powering the planet: Chemical challenges in solar energy utilization. 2006. [Online]. Available: 10.1073pnas.0603395103

3. M.G. Panthani et al., Synthesis of CuInS$_2$, CuInSe$_2$, and Cu(In$_x$Ga$_{1-x}$)Se$_2$ (CIGS) nanocrystal 'inks' for printable photovoltaics. J. Am. Chem. Soc. (2008). https://doi.org/10.1021/ja805845q

4. S. Banu, S.J. Ahn, S.K. Ahn, K. Yoon, A. Cho, Fabrication and characterization of cost-efficient CuSbS2 thin film solar cells using hybrid inks. Solar Energy Mater. Solar Cells (2016). https://doi.org/10.1016/j.solmat.2016.02.013

5. G. Surucu, K. Colakoglu, E. Deligoz, N. Korozlu, Y.O. Ciftci, The electronic and optical properties on the Zn$_{1-X}$Ca$_X$Se mixed alloys. Solid state Commun. **150**, 141–1428 (2010). https://doi.org/10.1016/j.ssc.2010.04.026

6. O. Bayrakli, M. Terlemezoglu, H.H. Güllü, M. Parlak, Investigation of precursor sequence and post-annealing effects on the properties of Cu$_2$SnZnSe$_4$ thin films deposited by the elemental thermal evaporation. Mater. Res. Express (2017). https://doi.org/10.1088/2053-1591/aa852d

7. H.H. Güllü, Ö. Bayraklı, M. Parlak, Optical and electrical characteristics of thermally evaporated Cu0.5Ag0.5InSe2 thin films. Thin Solid Films (2017). https://doi.org/10.1016/j.tsf.2017.08.024

8. G. Surucu, K. Colakoglu, E. Deligoz, Y. Ciftci, N. Korozlu, Electronic, elastic and optical properties on the Zn$_{1-x}$Mg$_x$Se mixed alloys. J. Mater. Sci. (2011). https://doi.org/10.1007/s10853-010-4864-y

9. F. Alharbi, J.D. Bass, A. Salhi, A. Alyamani, H.C. Kim, R.D. Miller, Abundant non-toxic materials for thin film solar cells: alternative to conventional materials. Renew. Energy **36**(10), 2753–2758 (2011). https://doi.org/10.1016/j.renene.2011.03.010

10. N. Khemiri, S. Chamekh, M. Kanzari, Properties of thermally evaporated CZTS thin films and numerical simulation of earth abundant and non toxic CZTS/Zn(S, O) based solar cells. Sol. Energy **207**, 496–502 (2020). https://doi.org/10.1016/j.solener.2020.06.114

11. K. Yu, E.A. Carter, A strategy to stabilize kesterite CZTS for high-performance solar cells. Chem. Mater. **27**(8), 2920–2927 (2015). https://doi.org/10.1021/acs.chemmater.5b00172

12. R. Nandi et al., Vapor-transport-deposited orthorhombic-SnSe thin films: a potential cost-effective absorber material for solar-cell applications. Solar RRL (2022). https://doi.org/10.1002/solr.202100676

13. A. Mavlonov et al., A review of Sb$_2$Se$_3$ photovoltaic absorber materials and thin-film solar cells. Sol. Energy **201**, 227–246 (2020). https://doi.org/10.1016/j.solener.2020.03.009

14. D.J. Xue et al., CuSbSe$_2$ as a potential photovoltaic absorber material: studies from theory to experiment. Adv. Energy Mater. (2015). https://doi.org/10.1002/aenm.201501203

15. R. Indirajith, M. Rajalakshmi, R. Gopalakrishnan, K. Ramamurthi, Effects of annealing on thermally evaporated SnSe thin films. Ferroelectrics **413**(1), 108–114 (2011). https://doi.org/10.1080/00150193.2011.551090

16. A.P. Torane, C.H. Bhosale, Preparation and characterization of electrodeposited Sb$_2$Se$_3$ thin films from non-aqueous media. J. Phys. Chem. Solids **63**, 1849–1855 (2002). https://doi.org/10.1016/S0022-3697(02)00167-1

17. D. Colombara, L.M. Peter, K.D. Rogers, J.D. Painter, S. Roncallo, Formation of CuSbS$_2$ and CuSbSe$_2$ thin films via chalcogenisation of Sb-Cu metal precursors. Thin Solid Films **519**(21), 7438–7443 (2011). https://doi.org/10.1016/j.tsf.2011.01.140

18. T.M. Razykov, A.X. Shukurov, O.K. Atabayev, K.M. Kuchkarov, B. Ergashev, A.A. Mavlonov, Growth and characterization of Sb$_2$Se$_3$ thin films for solar cells. Sol. Energy **173**, 225–228 (2018). https://doi.org/10.1016/j.solener.2018.07.082

19. K. Yang, B. Li, G. Zeng, Structural, morphological, compositional, optical and electrical properties of Sb$_2$Se$_3$ thin films deposited by pulsed laser deposition. Superlattices Microstruct. (2020). https://doi.org/10.1016/j.spmi.2020.106618

20. C. Chen et al., Characterization of basic physical properties of Sb$_2$Se$_3$ and its relevance for photovoltaics. Front. Optoelectron. **10**(1), 18–30 (2017). https://doi.org/10.1007/s12200-017-0702-z

21. X. Hu et al., Improving the efficiency of Sb2Se3 thin-film solar cells by post annealing treatment in vacuum condition. Sol. Energy Mater. Sol. Cells **187**, 170–175 (2018). https://doi.org/10.1016/j.solmat.2018.08.006

22. T.M. Razykov et al., Characterisation of SnSe thin films fabricated by chemical molecular beam deposition for use in thin film solar cells. Sol. Energy **159**, 834–840 (2018). https://doi.org/10.1016/j.solener.2017.11.053

23. N.D. Boscher, C.J. Carmalt, R.G. Palgrave, I.P. Parkin, Atmospheric pressure chemical vapour deposition of SnSe and SnSe$_2$ thin films on glass. Thin Solid Films **516**(15), 4750–4757 (2008). https://doi.org/10.1016/j.tsf.2007.08.100

24. D. Shikha, V. Mehta, J. Sharma, R.P. Chauhan, Effect of deposition temperature on structural, optical and electrical properties of nanocrystalline SnSe thin films. J. Mater. Sci.: Mater. Electron. **28**(3), 2487–2493 (2017). https://doi.org/10.1007/s10854-016-5822-5

25. K.S. Urmila, T.A. Namitha, J. Rajani, R.R. Philip, B. Pradeep, Optoelectronic properties and Seebeck coefficient in SnSe thin films. J. Semicond. (2016). https://doi.org/10.1088/1674-4926/37/9/093002

26. Z. Li et al., Effect of film thickness and evaporation rate on co-evaporated SnSe thin films for photovoltaic applications. RSC Adv **10**(28), 16749–16755 (2020). https://doi.org/10.1039/d0ra01749c

27. D. Pathinettam Padiyan, A. Marikani, K.R. Murali, Electrical and photoelectrical properties of vacuum deposited SnSe thin films. Cryst. Res. Technol **35**(8), 49–957 (2000). https://doi.org/10.1002/1521-4079(200008)35:83.0.CO;2-R

28. T. Bektas, M. Terlemezoglu, O. Surucu, M. Isik, M. Parlak, Growth and optical characterization of Sn0.6Sb0.4Se layer single crystals for optoelectronic applications. Mater. Sci. Semicond. Process. (2022). https://doi.org/10.1016/j.mssp.2021.106434

29. F.H. Aragón, Structural and surface study of praseodymium-doped SnO$_2$ nanoparticles prepared by the polymeric precursor method. J. Phys. Chem. C **119**(16), 8711–8717 (2015). https://doi.org/10.1021/acs.jpcc.5b00761

30. M. Parlak and C. Erçelebi, The effect of substrate and post-annealing temperature on the structural and optical properties of polycrystalline InSe thin films. Thin Solid Films **322**, 334–339 (1998). https://doi.org/10.1016/S0040-6090(97)00929-2

31. X. Tong, G. You, Y. Ding, H. Xue, Y. Wang, W. Guo, Effect of grain size on low-temperature electrical resistivity and thermal conductivity of pure magnesium. Mater. Lett. **229**, 261–264 (2018). https://doi.org/10.1016/j.matlet.2018.07.037

32. P.S. Satheesh Kumar, R. Sangeetha, R. Sivakumar, L. Amalraj, "Effects of substrate temperature on structural and optoelectronic properties of SnSe thin films by nebulized spray deposition for solar cell applications. Mater. Today Proc. **37**(Part 2), 2763–2769 (2020). https://doi.org/10.1016/j.matpr.2020.08.642

33. Z.J. Chen, T. Shen, R.K. Nutor, S.D. Yang, H.F. Wu, J.X. Si, Influence of local heterojunction on the thermoelectric properties of

Mo-SnSe multilayer films deposited by magnetron sputtering. J Electron Mater **48**(2), 1153–1158 (2019). https://doi.org/10.1007/s11664-018-06849-1

34. A. Kumar, V. Kumar, A. Romeo, C. Wiemer, G. Mariotto, Raman spectroscopy and in situ XRD probing of the thermal decomposition of Sb_2Se_3 thin films. J. Phys. Chem. C **125**(36), 19858–19865 (2021). https://doi.org/10.1021/acs.jpcc.1c05047

35. X. Gong et al., Temperature dependence of Raman scattering in single crystal SnSe. Vib Spectrosc. (2020). https://doi.org/10.1016/j.vibspec.2020.103034

36. J. Ge, Y. Yu, Y. Yan, Earth-abundant orthorhombic $BaCu_2Sn(Se_xS_{1-x})4$ ($x \approx 0.83$) thin film for solar energy conversion. ACS Energy Lett. **1**(3), 583–588 (2016). https://doi.org/10.1021/acsenergylett.6b00324

37. M. Demir, H.H. Gullu, M. Terlemezoglu, M. Parlak, Fabrication of $CdSe_xTe_{1-x}$ thin films by sequential growth using double sources. Phys. B Condens. Matter (2021). https://doi.org/10.1016/j.physb.2021.413232

38. S. Delice et al., Temperature dependence of band gaps in sputtered SnSe thin films. J. Phys. Chem. Solids **131**, 22–26 (2019). https://doi.org/10.1016/j.jpcs.2019.03.004

39. B.Y. Oh, M.C. Jeong, D.S. Kim, W. Lee, J.M. Myoung, Post-annealing of Al-doped ZnO films in hydrogen atmosphere. J. Cryst. Growth **281**(2–4), 475–480 (2005). https://doi.org/10.1016/j.jcrysgro.2005.04.045

40. N. Suri, K.S. Bindra, R. Thangaraj, Electrical conduction and photoconduction in $Se_{80-x}Te_{20}Bi_x$ thin films. J. Phys. Condens. Matter **18**(39), 9129–9134 (2006). https://doi.org/10.1088/0953-8984/18/39/038